IOP Publishing and International Atomic Energy Agency Nuclear Fusion
Nucl. Fusion **47** (2007) 1552–1558 doi:10.1088/0029-5515/47/11/017

Electron Bernstein wave heating of over-dense H-mode plasmas in the TCV tokamak via O-X-B double mode conversion

A. Pochelon[1], A. Mueck[1], L. Curchod[1], Y. Camenen[1], S. Coda[1], B.P. Duval[1], T.P. Goodman[1], I. Klimanov[1], H.P. Laqua[2], Y. Martin[1], J.-M. Moret[1], L. Porte[1], A. Sushkov[3], V.S. Udintsev[1], F. Volpe[2] and the TCV Team

[1] Ecole Polytechnique Fédérale de Lausanne (EPFL), Centre de Recherches en Physique des Plasmas, Association EURATOM-Confédération Suisse, CH-1015 Lausanne, Switzerland
[2] Max Planck Institut für Plasmaphysik, IPP-Greifswald, D-17491 Greifswald, Germany
[3] RRC 'Kurchatov Institute', Nuclear Fusion Institute, 123182 Moscow, Russia

E-mail: Antoine.Pochelon@epfl.ch

Received 10 January 2007, accepted for publication 22 August 2007
Published 19 October 2007
Online at stacks.iop.org/NF/47/1552

Abstract
This paper reports on the first demonstration of electron Bernstein wave heating (EBWH) by double mode conversion from ordinary (O-) to Bernstein (B-) via the extraordinary (X-) mode in an over-dense tokamak plasma, using low field side launch, achieved in the TCV tokamak H-mode, making use of its naturally generated steep density gradient. This technique offers the possibility of overcoming the upper density limit of conventional EC microwave heating. The sensitive dependence of the O-X mode conversion on the microwave launching direction has been verified experimentally. Localized power deposition, consistent with theoretical predictions, has been observed at densities well above the conventional cut-off. Central heating has been achieved, at powers up to two megawatts. This demonstrates the potential of EBW in tokamak H-modes, the intended mode of operation for a reactor such as ITER.

PACS numbers: 52.55.ñs, 52.55.Fa, 52.50.Gj, 52.50.ñb, 52.50.Sw, 52.35.Hr, 52.35.Mw

(Some figures in this article are in colour only in the electronic version)

1. Introduction

A high plasma density is beneficial to the fusion power yield in a thermonuclear reactor both directly, by increasing the reaction rate, and indirectly, by increasing the plasma confinement, according to well-established experimental scaling laws. The heating of high-density plasmas with electron cyclotron resonance heating (ECRH) is, however, limited by the reflection of the microwaves at so-called wave cut-offs [1]. In contrast, the electrostatic Bernstein mode encounters no density cut-off in the plasma, but cannot propagate in vacuum and must thus be excited by mode conversion. The double mode conversion scheme from the O-mode to the X-mode and finally to the Bernstein mode (O-X-B) is examined in this paper [2, 3].

The accessibility of EC waves depends primarily on the magnetic field of the device, determining the frequency of the power sources. We compare the EC waves accessibility in tokamak-like machines, from the low field spherical tokamaks ($B = 0.5$ T), through medium field TCV ($B = 1.5$ T, $R = 0.88$ m, $a = 0.25$ m), to the high field ITER machine ($B = 5.3$ T) [4]. The accessibility limitation due to EC cut-offs has to be compared with the empirical tokamak density limit, the Greenwald density limit $< n_{eG} >= 0.27 \cdot I_p/a^2$ [5], where I_p is the plasma current and a the plasma radius. For this comparison, the value of I_p for the different devices is taken using the shaping parameters, elongation and triangularity and safety factor from the standard ITER operation model (q_{95}=3, $\kappa = 1.85$, $\delta = 0.5$).

In spherical tokamaks, the low EC harmonics may only access densities up to a few per cent of n_{eG}, so that another heating scheme such as EBW has great potential. In the medium field machine TCV, 10% of n_{eG} is accessible with the 2nd harmonic X-mode (X2), which has been successfully

extended to 25% using the 3rd harmonic X-mode (X3) [6]. The density range above O2 and X3 cut-off density limits can be accessed with EBWs, for instance using the 2nd harmonic as described in this paper. In ITER, the magnetic field is sufficiently high to permit heating of the intended operational density range using the fundamental O-mode (O1) at 170 GHz. Current drive applications using EBWs, however, which are potentially more efficient than ECCD [7–10] yet benefiting from the same localized deposition properties, could make EBW even more attractive.

In the conversion scheme used, an elliptically polarized O-mode wave is injected at a particular angle, converts at the plasma cut-off into the X-mode, and propagates back to the upper hybrid resonance. Close to this resonance, the X-mode converts into the electrostatic Bernstein mode, which then propagates towards the plasma centre where it is absorbed at harmonics of the EC resonance. For a hot plasma, this second conversion has an efficiency of ∼100% (in the absence of parametric decay effects). The O- to X-mode conversion efficiency, however, depends on the O-mode wave injection angle and may be characterized by the power transmission function T from the O- to the X-mode, derived by Mjølhus [11]:

$$T(N_\perp, N_{||}) = \exp(-\pi k_0 L_n (Y/2)^{1/2} \times [2(1+Y)(N_{||,\mathrm{opt}} - N_{||})^2 + N_\perp^2]) \quad (1)$$

with $k_0 L_n = k_0 n_e/(\partial n_e/\partial x)$ the radial normalized density-gradient scale length at the cut-off density, $k_0 = 2\pi/\lambda_0$ being the wave number of the incident wave in vacuum and λ_0 the free space wavelength, with the refraction indices perpendicular $N_\perp$ and parallel $N_{||}$ to the local magnetic field and $Y = \omega_{ce}/\omega$, where ω_{ce} is the electron cyclotron frequency and ω the wave frequency. Only at the optimum refractive indices $N_{||}^2 = N_{||,\mathrm{opt}}^2 \equiv Y/(Y+1)$ to an optimum injection angle, can the O-mode wave be completely converted to the X-mode. For non-optimal injection angles, the O-X conversion efficiency decreases with increasing L_n. The wave energy that is not mode converted reflects back towards the plasma edge and either escapes the plasma or contributes via multi-pass absorption.

This heating scheme is not new. Electron Bernstein wave heating (EBWH), using the O-X-B double mode conversion scheme, was successfully demonstrated in the W7-AS stellarator [12], with injection into a high density high (HDH) confinement mode. Electron Bernstein emission (EBE) measurements in spherical, low aspect-ratio tokamaks and in reversed field pinches are reported in [13–15]. High field side (HFS) launch Bernstein wave heating was demonstrated in a tokamak using the X-B scheme [16], but this scheme is limited by the left-hand X-mode cut-off in practical applications. Over-dense plasma heating was demonstrated in a spherical tokamak using the X-B scheme from the low field side (LFS) with the X-mode tunnelling through the evanescent layer and with L_n artificially reduced by a local limiter [17]. The experiments in TCV [18–21], however, demonstrate EBWH for the first time in an over-dense plasma of standard aspect-ratio tokamak, with O-X-B double mode conversion, with the required low L_n values (high-density gradient) obtained in the high-confinement mode (H-mode) [22].

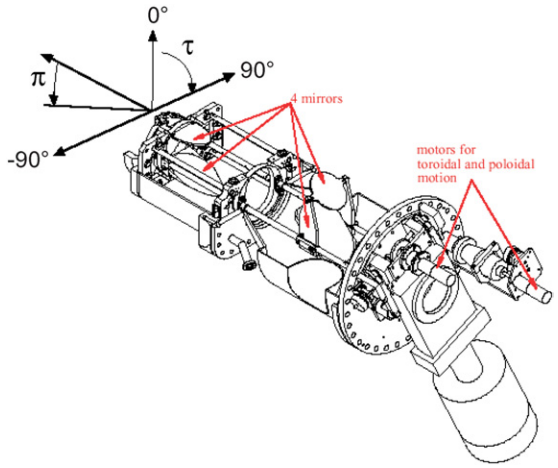

Figure 1. EC launcher system, composed of four mirrors, with the last mirror before the plasma on the left. The 2 degrees of freedom of the launcher are represented by the two angles τ (rotation of the whole mirror set-up around its axis) and π (swing of the last mirror).

2. Experimental set-up

2.1. TCV ECH system and diagnostics

The TCV tokamak is equipped with 4.5 MW ECH nominal power for pulse lengths of 2 s: 3 MW at the 2nd harmonic (X2 system, any polarization) and 1.5 MW at the 3rd harmonic (X3 system, 118 GHz not used here). The X2/O2 system features six 500 kW gyrotrons at a frequency of 82.7 GHz equipped with six LFS launchers installed on the upper lateral (4) and equatorial ports (2). All six launchers are independently steerable during the discharge, each with two degrees of freedom, the two so-called 'launcher angles' τ and π, parametrizing the beam directions, as depicted in figure 1. The angle τ is generated by a rotation of the four-mirror system around its axis, whereas the angle π is generated by a tilt of the last mirror steering the beam to the plasma. This last mirror is focusing, with a beam divergence of 2° and a beam waist located at 0.13 m from the last mirror, very close to the intersection of the EC beam with the last closed flux surface in typical EBWH conditions. The required elliptical polarization to maximize the coupling of the EC wave at the plasma edge is calculated from the plasma equilibrium and launcher edges installed before the discharge [23].

At the axial TCV magnetic field of $B = 1.5$ T, the cut-off densities for X2, O2 and X3 waves are 4.2, 8.7 and 11.1 × 10^{19} m^{-3}, respectively. This paper explores the potential of high power EBW at densities above the O2 cut-off density, required for the O-X conversion scheme, and up to densities largely in excess of X3 cut-off. Three diagnostics are used to measure the power absorption. The reflected EC power, scattered inside the torus, is measured by a few semiconductor diodes, installed in different sectors of TCV [24]. Using power modulation techniques [25], the total absorbed power is measured by a diamagnetic loop (DML) [18] and the local deposition [20,21] is measured with a high spatial resolution, 64-channel, soft x-ray wire chamber (DMPX) viewing the plasma vertically, with a krypton gas fill and sensitive in the 2–25 keV range (10% efficiency limits) [26].

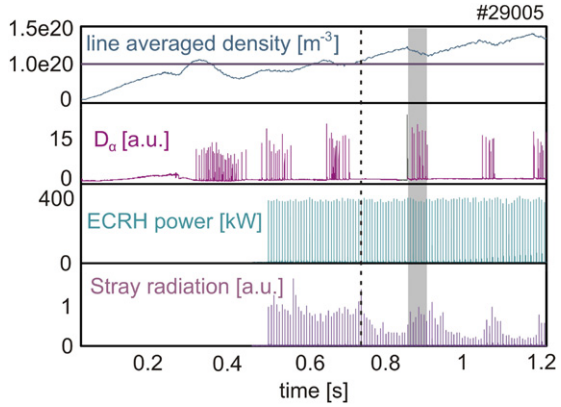

Figure 2. Typical high-density ELMy H-mode target plasma with alternating ELM-free phases. Modulated EC waves are injected. When the plasma becomes over-dense, the stray level becomes low in the ELM-free phases (indicated by the vertical dotted line), indicating increased O-X power conversion, and higher in the ELMy phases. The highlighted region is detailed in figure 3.

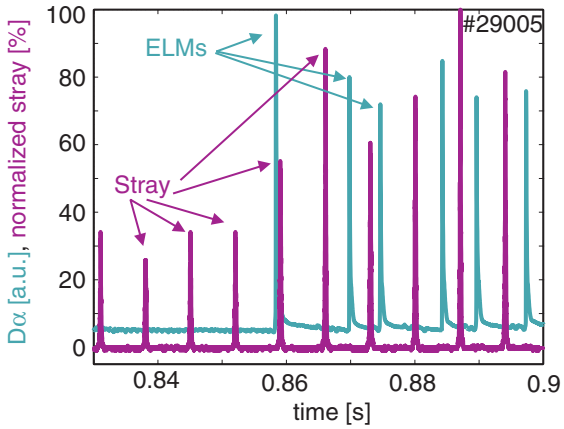

Figure 3. Stray radiation power normalized to its maximum value during the shot (violet) and D_α-light emission (green). The presence of ELMs can strongly influence the stray radiation. The stray power, measured during the short EC pulses, rises from 30% during the ELM-free phase to 80% during the ELM phase (after 0.856 s).

2.2. Optimization of H-mode discharges for EBW coupling

To achieve a large angular window of the O-X power transmission function, the density scale length at the plasma cut-off must be reduced, implying a steep density gradient (small L_n), see equation (1). This is available in the edge pedestal of TCV H-mode plasmas typically with low $q_{95} = 2.2$–2.4, high triangularity $\delta = 0.5$–0.6, and medium elongation $\kappa = 1.8$ (with $I_p = 415\,\mathrm{kA}$, $1.2 < B < 1.4\,\mathrm{T}$, $n_{eo} \geqslant 1 \times 10^{20}\,\mathrm{m}^{-3}$ equivalent with $n_{eo}/n_{eoG} \sim 0.4$–0.6). Low q, high δ, high n_e and high power are known to favour H-mode pedestals with high edge density gradients and thus low L_n [27]. Low-q H-modes, however, often exhibit strong MHD activity: large central sawteeth and edge localized modes (ELMs). Strong core activity can hamper the diagnostics measuring local power deposition in the plasma centre. To date, the most successful target discharges for the demonstration of EBWH in TCV are non-stationary, with the density continually increasing in average.

For these discharges, the O2 density cut-off typically occurs at $\rho_\psi \sim 0.9$, in the steep-edge-density gradient region and the plasma centre is over-dense with a typical value of $(\omega_{pe0}/\omega)^2 \sim 1.7$. Data from a typical high-density target plasma is shown in figure 2, with the D_a exhibiting alternating ELMy/ELM-free phases. The line-averaged density and density gradient are both increasing during the ELM-free phases and dropping during the ELMy phase. To avoid producing any perturbation of the H-mode in the case of non-optimal injection angle, 500 kW modulated EC power was first injected in pulses of 0.2 ms (FWHM) at a low duty cycle of 3%. The stray radiation level is normalized to its maximum value at lower density during the discharge and plotted in figure 2. It decreases with rising density in the ELM-free phase, indicating an increase in EC power absorption. Conversely the stray level is observed to rise rapidly with the occurrence of the first ELMs, see figure 3, suggesting diminished EC wave conversion, presumably caused by the ELM induced decrease in both the global electron density and the local density gradient at the O-mode cut-off. This is illustrated by the change in the Thomson scattering density profile shown in figure 4. The trend in density profile erosion with ELMs is further confirmed in TCV by high-spatial-resolution edge Thomson scattering measurements in similar H-mode discharges but performed at a different vertical plasma axis location and substantially lower density [28].

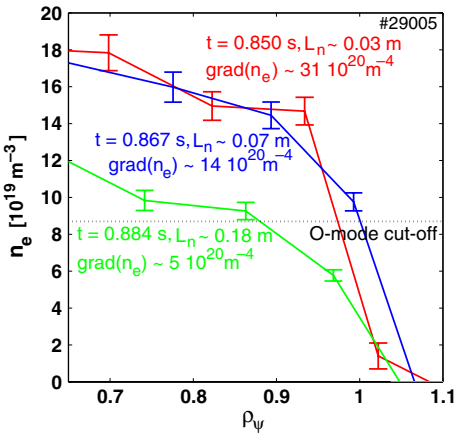

Figure 4. Erosion of the density profiles at the onset of an ELM phase for the case of figure 3, indicating an increase in the density scale length at the O-mode cut-off density with the occurrence of the first ELMs. Three density profiles are shown: (1) ELM-free phase (0.850 s, red), (2) after the first ELM (0.867 s, blue), (3) after the third ELM (0.884 s, green).

3. Experimental determination of optimum injection angle

A single ray simulation with the non-relativistic ART ray tracing code [29–31], which includes O-X-B double mode conversion for wave propagation and absorption, was first performed for the target plasma conditions, to estimate the optimal poloidal and toroidal injection angles.

Around these simulated optimal angles, experimental scans along the two 'launcher angles' τ and π, (keeping the

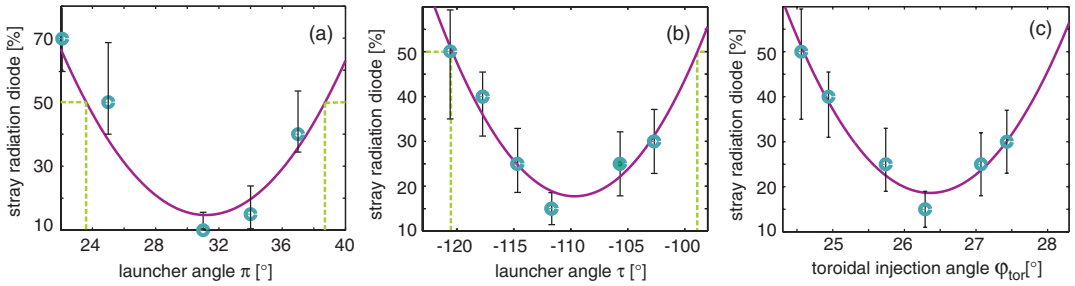

Figure 5. (*a*) Normalized stray radiation power versus 'launcher angle' π (maintaining τ constant) and (*b*) versus τ (maintaining π constant) and (*c*) the same last scan projected on the toroidal injection angle $\varphi_{\rm tor}$. The solid curves represent polynomial regression fits to the data points. The dashed lines in (*a*) and (*b*) indicate the width of 50% of the maximum stray level. This width is about twice the ART single ray calculation width, as shown in figure 6.

other angle fixed) were performed on a shot to shot basis to measure the plasma reaction. For an equatorial launch clear minima in the stray radiation level are found during this scan, see figures 5(*a*) and (*b*), indicating the power absorption maxima and thus yielding a measure of the optimal angles. These angles are the converted in toroidal and poloidal injection angles ($\varphi_{\rm tor}$ and $\varphi_{\rm pol} = 0$ for an injection in the poloidal plane and in the horizontal direction, respectively). The optimum toroidal angle is then found to be approximately 26°, see figure 5(*c*). Comparable launch angle dependence in the stray radiation is found for both launcher angles on all stray radiation diode signals around the torus and for different poloidal launcher positions, that is, for both upper lateral and equatorial launchers.

The experimentally determined optimum angles are now compared with the ART ray tracing code results. In figure 6, the simulated O-X conversion efficiency is shown in a contour plot. The innermost contour indicates 90% conversion, the outermost contour 10%. The converted experimental angles of the τ- and π-scans for the equatorial port launch are indicated as violet dots and the extrapolated optimum angle as a green dot. This experimental optimum angle is in good agreement with the simulated angle. This small discrepancy ($<2^\circ$) can have its origin partly in the resolution of the scans (3° between the experimental points) but mostly in the imprecision of the magnetic equilibrium reconstruction of $\sim \pm 1$ cm. When such an equilibrium shift is applied to the ART simulation, the optimum angles shift typically by $\sim \pm 1^\circ$.

The experimentally determined, 50%-absorption width shown in figures 5(*a*) and (*b*) are also indicated in figure 6. These experimental absorption widths are larger than the simulation widths by typically a factor of two. The discrepancy between this measured and calculated angular window size (50% contours) is not surprising in view of the finite width of the EC beam and the spread in its wave-number spectrum. Both are expected to broaden the width of the conversion efficiency function and reduce its absolute value. This is also consistent with a measurable minimum stray level, implying that less than 100% of the beam power is absorbed.

In summary, the angular dependence and the agreement of the optimal angles between experiment and simulation strongly indicate that O-X-B mode conversion is occurring [18–21].

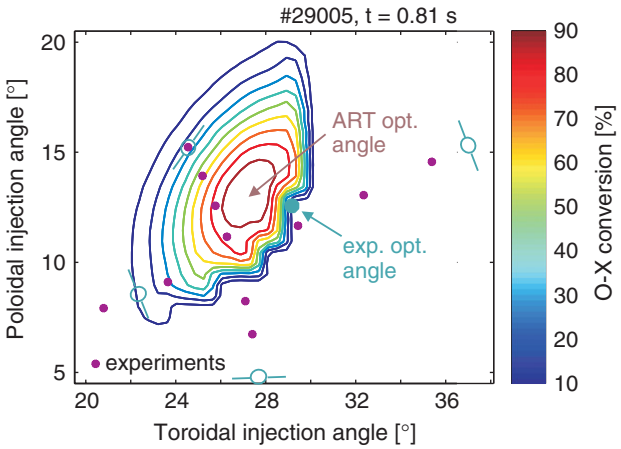

Figure 6. Contour plot of calculated O-X power conversion efficiency versus toroidal and poloidal injection angles ($\varphi_{\rm tor}$ and $\varphi_{\rm pol}$). The contours are equi-spaced, the innermost contour indicating 90% O-X conversion, the outermost 10%. The superimposed points give the angles of the experimental scans (see figures 5(*a*) and (*b*)). The green point corresponds to the extrapolated optimum experimental angles and is within 2° of the calculated optimum angles. The measured 50% stray radiation level is indicated along the experimental angle scans, denoted by four circles.

4. Global and local Bernstein wave heating

Heating experiments were performed with the experimentally determined optimal angles. The duty cycle was increased to 46% with ~500 kW EC power injected for a modulation frequency of 182 Hz. This modulation frequency was chosen between the 1st (~110 Hz) and 2nd harmonics of the sawtooth instability, to diminish the perturbative effect of the sawteeth on the FFT analysis.

A basic cross-check of the O-X transmission can be performed by comparing the stray radiation levels when power is injected in the vicinity of the optimum angles, first in O- then in X-mode. For a similar ELM-free phase with the same EC power, the stray level for O-mode injection was only 40% of that observed for X-mode injection, showing that considerably higher absorption due to mode conversion is obtained with O-mode injection.

The overall absorbed power was determined with a DML [20], which measures the toroidal magnetic flux variation

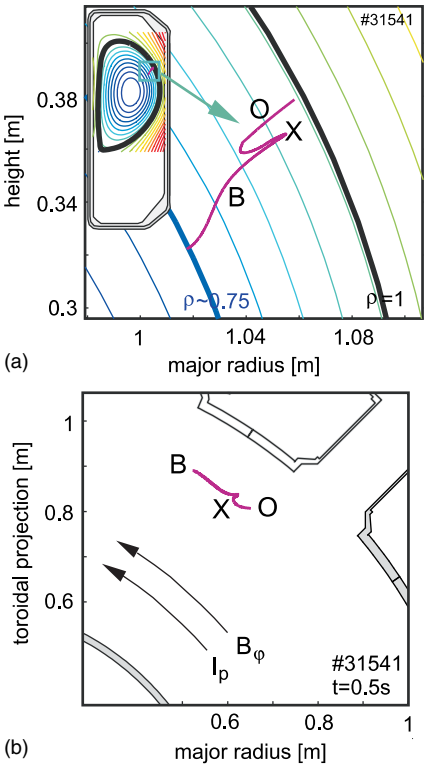

Figure 7. ART ray tracing calculation of the wave path in (*a*) poloidal and (*b*) toroidal projections, including O-X-B double mode conversion.

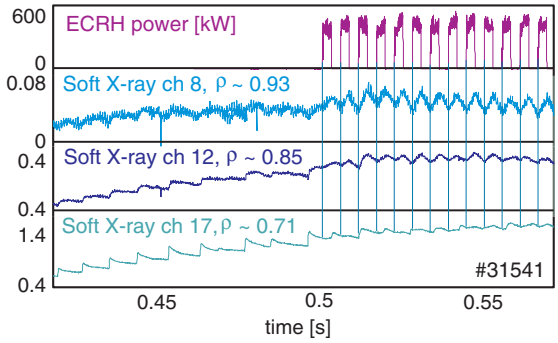

Figure 8. The injection of modulated EC waves is directly visible on several radial soft x-ray time traces. On the two outer channels shown here, the signal is dominated by the EC modulation frequency. On the innermost channel shown on the bottom, the EC pulses only modify the sawtooth slope. To determine the deposition location, an FFT of the time trace of each channel is performed.

directly related to the plasma stored energy. Absorption of typically 60% was obtained for O-mode injection whereas for X-mode injection, the absorption was below 10%. O-mode waves must therefore mode convert and then penetrate further into the plasma while X-mode waves are reflected back, as expected for over-dense plasmas. A total power absorption measurement cannot be used to conclusively prove the nature of the absorption mechanism, which could also involve edge absorption of waves generated by nonlinear wave–wave coupling and/or absorption of waves multiply reflected at the vacuum vessel. A determination of the power deposition location is therefore essential to prove EBW heating.

The plasma centre of the high-density target plasma is strongly affected by the sawtooth instability, which repeatedly expels high power heat pulses from the hot plasma core towards the colder edge region. In the core of the plasma close to this strong instability, proving power deposition from EBWH is rather difficult. Therefore conditions for a power deposition location off-axis, but still well inside the plasma cut-off, were selected. In figure 7, an ART simulation of such a wave path is shown in poloidal and top view projections, for the case of an upper lateral port launch. The O-mode wave propagates to the plasma cut-off, is mode converted in the X-mode and then returns to the upper hybrid resonance where it is converted in a Bernstein wave. The B wave is then calculated to be absorbed at $\rho_\psi \sim 0.78$, well inside the plasma cut-off layer located at $\rho_\psi \sim 0.9$ (see figure 9(*b*)).

The power deposition location is determined experimentally using the soft x-ray emission measured by a high-spatial-resolution multi-wire proportional detector (DMPX) with its lines of sight in the vertical direction, covering the entire plasma cross-section, and viewing the plasma through a total beryllium thickness of 100 μm. For these conditions the soft x-ray emissivity increases monotonically with the electron temperature and density. In figure 8, the heating effect caused by the modulated EC power is visible in the line-integrated time traces of several channels, on both the HFS and the LFS. The deposition location is first evaluated using FFT analysis of the 64 soft x-ray chord signals. The FFT amplitude at the EC modulation frequency is plotted against the soft x-ray channel number in figure 9(*a*). Two clear amplitude maxima are visible. These broad spatial maxima correspond to emission at $\rho_\psi \sim 0.65$, on both the HFS and the LFS. The maximum on the HFS is more pronounced due to the geometrical effects of line integration and field line compression with positive plasma triangularity.

To remove the effect of line-integration of the local soft x-ray emissivity, the profile is inverted. This is accomplished with a tomographical inversion assuming poloidal homogeneity and imposing the Fisher regularization algorithm [32, 33]. Figure 9(*b*) plots the FFT amplitude of the inverted data at the EC modulation frequency against the poloidal flux radial coordinate ρ_ψ. The radial maximum of the FFT amplitude, after inversion, is located at $\rho_\psi \sim 0.71$, well inside the plasma cut-off. The absorption occurs in fact at a density of $n_e \sim 1.32 \times 10^{20}\,\mathrm{m}^{-3}$, which is over-dense with a value of $(\omega_{pe}/\omega)^2 \sim 1.5$. The experimental radial deposition location is close to that calculated with ART (single ray), at $\rho_\psi \sim 0.78$; i.e. within 10% of the radial coordinate. The slight difference may again be attributed to uncertainties in the equilibrium reconstruction and the density gradient measurement. In addition, the edge soft x-ray signals indicate some residual power deposited outside cut-off, presumably resulting from 2nd harmonic X-mode absorption of non-O-X-B-converted wave power absorbed after multiple wall reflections and mode scrambling.

Again, the good agreement between the theoretical and experimental radial deposition locations, together with deposition at an over-dense location, constitutes strong proof that the O-X-B conversion mechanism is at work.

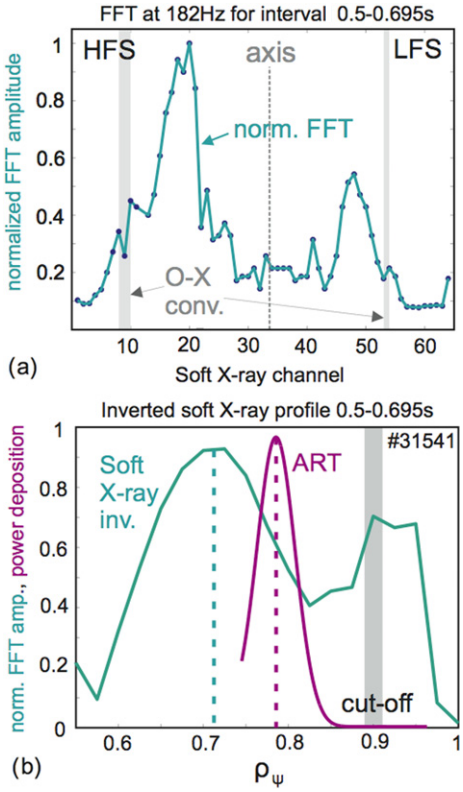

Figure 9. (*a*) Normalised FFT amplitude of the line-integrated soft x-ray time traces at the modulation frequency (182 Hz) of the injected EC waves, versus chord number. (*b*) normalised FFT amplitude of the local soft x-ray emissivity at the modulation frequency, derived by inversion of the line-integrated soft x-ray chord signals (green) demonstrating over-dense deposition at $\rho_\psi \sim 0.71$. The normalized density of the deposited beam power, calculated with single ray ART calculation (violet), is also indicated confirming EBW absorption well inside the cut-off at $\rho_\psi \sim 0.78$.

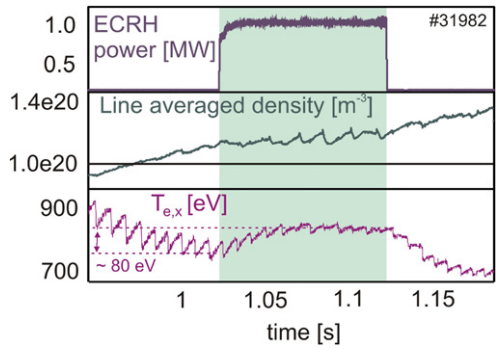

Figure 10. Long 1 MW EC power modulation pulses of 100 ms, on top of 1 MW CW (not shown), demonstrating a temperature increase due to EBWH, measured by the soft x-ray absorber method. With the essentially constant density, the temperature increase can be attributed to EBWH.

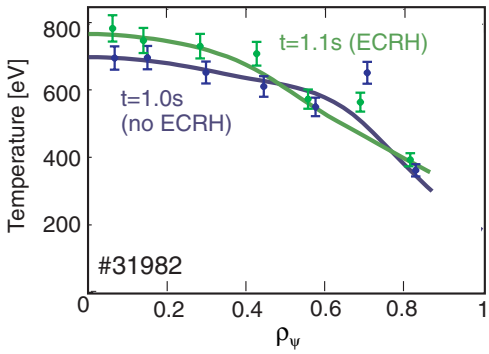

Figure 11. Electron temperature profiles before the modulation EC power pulse (1.0 s) and during the modulation EC pulse (1.1 s), from the Thomson scattering, confirming the central electron temperature increase measured from soft x-rays, figure 10.

5. Central electron temperature increase by long pulse EBWH

To be able to observe EBH effects such as an increase in the central temperature, the pulse duration was extended to 100 ms, i.e. over several energy confinement times ($\tau_E \sim 50$ ms), and the power increased to 2 MW with a modulation depth of 1 MW, as shown in figure 10. Here, four independent launchers were employed. The injection angles were chosen such that both upper lateral and equatorial launchers heat at the same location at $\rho_\psi \sim 0.4$ (calculated by ART), where $(\omega_{pe}/\omega)^2 \sim 1.5$. Particular care was taken to ensure that the two modulated beam locations coincided. This more central deposition was achieved by lowering the machine magnetic field to 1.2 T to displace the 2nd harmonic cold resonance further to the HFS.

TCV is equipped with three centrally aimed soft x-ray diodes equipped with different beryllium thicknesses, which are used to measure the (centre-weighted) electron temperature with high temporal resolution by the absorber method. All diode combinations showed an increase in electron temperature of $\Delta T_e \sim 80$ eV during the EC pulse (figure 10). With the total injected power of 2 MW, large ELMs develop at a slow repetition rate (16 ms), resulting in a near constant plasma density (unlike the case with fast ELMs at lower injected power). The slowly increasing density during the pulse ensures that the temperature increase is directly attributable to an additional heating effect of EBW. The central temperature increase is also supported by the Thomson scattering measurements. Figure 11 shows two successive Thomson temperature profiles taken at 1.0 s (1 MW EC power), just before ECH modulation, and at 1.1 s during ECH modulation (2 MW EC power). The evident increase in the central electron temperature due to the additional 1 MW EC power is in agreement with the fast soft x-ray absorber measurement.

6. Conclusions and outlook

EBW heating by O-X-B double mode conversion in an over-dense plasma of standard aspect-ratio tokamak has been demonstrated in TCV. The optimal injection angles for O-X-B conversion were determined experimentally with 2D angle scans by minimizing the microwave stray radiation levels in discharges with low duty cycle modulated EC wave injection. Double mode conversion simulations with the ART ray tracing code were performed demonstrating excellent agreement between the simulated and measured optimal angles.

Higher duty cycle modulated EC waves were injected to measure global and local EBWH power deposition. A

global absorbed-power-fraction of ∼60% was measured from the diamagnetic probe with densities well above the cut-off. The spatial distribution of the local power absorption was determined experimentally by FFT analysis of soft x-ray emissivity signals. The deposition radius, well inside the plasma cut-off, matches the value predicted by ART within the experimental uncertainties. These modulated power deposition measurements were designed with a relatively far off-axis deposition, at $\rho_\psi \sim 0.7$, to avoid the strong sawtooth perturbations that hamper detection of the central power deposition. Long pulse power deposition, for periods of many confinement times, was achieved at a lowered magnetic field to obtain a more central power deposition, predicted at $\rho_\psi \sim 0.4$. Corroborating central electron temperature increases were found from both Thomson scattering and soft x-ray absorber measurements.

In summary, the experiments presented here demonstrate for the first time that EBWH of over-dense plasmas can be used in a standard aspect-ratio tokamak, in the H-mode, taking advantage of the naturally occurring steep density gradients.

Acknowledgments

This work was supported in part by the Swiss National Science Foundation. A. Mueck was supported by a EURATOM Fusion fellowship.

References

[1] Stix T.H. 1992 *Waves in Plasmas* (New York: Springer)
[2] Bernstein I.B. 1958 *Phys. Rev.* **109** 10
[3] Preinhaelter J. and Kopecký V. 1973 *J. Plasma Phys.* **10** 1
[4] Pochelon A. *et al* 2006 *Proc. 6th Int. Workshop on Strong Microwaves in Plasmas (Nizhny Novgorod, Russia, 2005)* vol 2 ed A.G. Litvak (Nizhny Novgorod: Russian Academy of Sciences, Institute of Applied Physics) p 421
[5] Greenwald M. *et al* 1988 *Nucl. Fusion* **28** 2199
[6] Porte L., Coda S. and Alberti A. 2007 *Nucl. Fusion* **47** 952
[7] Forest C.B., Chattopadhyay P.K., Harvey R.W. and Smirnov A.P. 2000 *Phys. Plasmas* **7** 1352
[8] Ram A.K., Decker J. and Peysson Y. 2005 *J. Plasma Phys.* **71** 675
[9] Shevchenko V., Baranov Y., O'Brien M. and Saveliev A. 2002 *Phys. Rev. Lett.* **89** 265005
[10] Laqua H.P. *et al* 2003 *Phys. Rev. Lett.* **90** 075003
[11] Mjølhus E. 1984 *J. Plasma Phys.* **31** 7
[12] Laqua H.P. *et al* 1997 *Phys. Rev. Lett.* **78** 3467
[13] Chattopadhyay P.K. *et al* 2002 *Phys. Plasmas* **9** 752
[14] Taylor G. *et al* 2005 *Phys. Plasmas* **12** 052511
[15] Shevchenko V. *et al* 2003 *15th Topical Conf. on Radio Frequency Power in Plasmas (Moran, WY)* ed C. Forest (Melville, NY: American Institute of Physics) *AIP Conf. Proc.* **694** 359
[16] McDermott F.S., Bekefi G., Hackett K.E., Levine J.S. and Porkolab M. 1982 *Phys. Fluids* **25** 1488
[17] Shiraiwa S. *et al* 2006 *Phys. Rev. Lett.* **96** 185003
[18] Mueck A. *et al* 2005 O-X-B mode conversion in the TCV tokamak *Proc. 32nd Eur. Conf. on Plasma Physics and Controlled Fusion (Tarragona, Spain)* P4.110
[19] Mueck A. *et al* 2007 *Phys. Rev. Lett.* **98** 175004
[20] Mueck A. *et al* 2006 Electron Bernstein wave heating in the TCV tokamak *14th Joint Workshop on ECE and ECRH (Santorini, Greece)* 2007 *Fusion Sci. Tech.* **52** 221
[21] Mueck A. *et al* 2006 Electron Bernstein wave heating in the TCV tokamak *Proc. 33rd Eur. Conf. on Plasma Physics and Controlled Fusion (Rome, Italy)* P1-153
[22] Wagner F. *et al* 1982 *Phys. Rev. Lett.* **49** 1408
[23] Goodman T.P., Alberti S., Henderson M.A., Pochelon A. and Tran M.Q. 1996 Design and installation of the electron cyclotron wave system for the TCV tokamak *19th Symp. on Fusion Technology (Lisbon, Portugal)* p 565
[24] Gandini F. *et al* 2001 *Fusion Eng. Des.* **56–57** 975
[25] Manini A. *et al* 2002 *Plasma Phys. Control. Fusion* **44** 139
[26] Sushkov A. *et al* 2002 TCV high resolution x-ray imaging diagnostic *Proc. 29th Eur. Conf. on Plasma Physics and Controlled Fusion (Montreux)* vol 26B (ECA) P-4.118
[27] Hughes J.W. *et al* 2002 *Phys. Plasmas* **9** 3019
[28] Behn R. *et al* 2007 *Plasma Phys. Control. Fusion* **49** 1289
[29] Volpe F. 2003 Electron Bernstein emission diagnostic of electron temperature profile at W7-AS stellarator *PhD Thesis* Ernst-Moritz-Arndt-Universität, Greifswald, Germany
[30] Volpe F. 2003 *PhD Thesis* Max-Planck Institut für Plasmaphysik, IPP Garching and Greifswald *IPP Report* 13/1
[31] Volpe F., Laqua H.P. and the W7-AS Team 2003 *Rev. Sci. Instrum.* **74** 1409
[32] Camenen Y. 2006 Étude du transport d'énergie thermique dans les plasmas du tokamak à configuration variable au moyen de chauffrage électronique cyclotronique *PhD Thesis* Swiss Federal Institute of Technology, Lausanne (EPFL), Switzerland, Thesis No 3618
[33] Camenen Y. 2006 *PhD Thesis* Swiss Federal Institute of Technology, Lausanne (EPFL), Centre de Recherches en Physique des Plasmas, CH-1015 Lausanne, Switzerland, Lausanne, Report LRP 821106